Step Change Detection for Improved ROCOF Evaluation of Power System Waveforms

Alexandra Karpilow, Mario Paolone
Distributed Electrical Systems Laboratory, EPFL
Lausanne, Switzerland
Alexandra.Karpilow@epfl.ch
Mario.Paolone@epfl.ch

Asja Derviškadić
Swissgrid Ltd.
Aarau, Switzerland
Asja.Derviskadic@swissgrid.ch

Guglielmo Frigo
METAS
Bern, Switzerland
Guglielmo.Frigo@metas.ch

***Abstract*—In the analysis of power grid waveforms, the presence of amplitude or phase steps can disrupt the estimation of frequency and rate-of-change-of-frequency (ROCOF). Standard methods based on phasor-models fail in the extraction of signal parameters during these signal dynamics, often yielding large frequency and ROCOF deviations. To address this challenge, we propose a technique that approximates components of the signal (e.g., amplitude and frequency variations) using dictionaries based on parameterized models of common signal dynamics. Distinct from a previous iteration of this method developed by the authors, the proposed technique allows for the identification of multiple steps in a window, as well as the presence of interfering tones. The method is shown to improve signal reconstruction when applied to real-world waveforms, as compared to standard static and dynamic phasor-based algorithms.**

***Index Terms*—Power system signals, amplitude and phase steps, dictionary analysis, power system measurements, rate of change of frequency (ROCOF)**

I. Introduction

Phasor Measurement Units (PMUs) are considered at the forefront of grid monitoring technology with fast and allegedly accurate measurements of waveform properties (e.g., frequency, rate-of-change-of-frequency (ROCOF), phase angle, etc.). However, fast variations in signal waveforms can significantly disturb phasor-based analysis, making the results invalid. In particular, step changes in the amplitude and/or phase of AC voltage or current waveforms, caused by network reconfigurations, circuit breaker operations or faults, can be misinterpreted as large deviations in the frequency inducing temporary high ROCOF estimations [1]. In distribution systems, this can lead to false triggering of loss-of-mains (LOM) protection [1] and errors in synthetic inertia calculations. For transmission systems, frequency and ROCOF are typically used for Under-Frequency Load Shedding (UFLS) actions to reduce the chance of cascading blackouts, generation loss or grid separation [2].

The IEEE Std. C37.118 [3] specifies performance requirements for PMUs when phase and amplitude step changes occur. As discussed in [4], a possible strategy to meet these requirements would be to apply Finite Impulse Response (FIR) or Kalman filters. The objective of these methods is to reject the presence of dynamic components for improved phasor estimation. However, recent literature has demonstrated that the phasor model may be inappropriate to deal with waveforms containing these types of events [5]. When signal dynamics like frequency ramps, phase/amplitude steps and amplitude modulations are present, the frequency spectrum of the waveform is broadband with energy distributed across many frequencies [1], [6]. The narrowband nature of the phasor model employed in PMUs makes it inherently unqualified to capture these signal dynamics and draws into question the validity of an "underlying" fundamental phasor [7]. Consequently, application of phasor-based methods to dynamic waveforms, particularly those with phase and amplitude steps, can yield misleading synchrophasor estimations and inappropriate control actions.

Recent literature discusses signal processing techniques to better analyze non-stationary waveforms from power grids. There is significant research on dynamic phasor methods based on Taylor series expansion or Taylor-Fourier series to approximate higher order phasor derivatives and broaden the bandwidth of the signal model [8], [9]. However, these methods are incapable of handling fast transients like amplitude or phase steps, as will be demonstrated in this paper.

Other strategies include detection of abrupt transients in order to flag the reported phasor as either invalid or in need of additional processing. In [10], a wavelet-based method is proposed to detect the presence of amplitude and phase steps in order to select between two phasor-based algorithms for stationary and dynamic signals. However, the suggested methods aim to dampen (or remove) the impact of the dynamic component rather than fully characterize it. Similarly, in [11] the event location is identified through wavelet analysis. The pre- and post-event data is then analyzed separately by fitting a quadratic polynomial to the waveforms with a linear regression process. The algorithm's performance when multiple steps or harmonics are present is not discussed. In [12], a Kalman Filter for waveform prediction is used to detect deviations of the input signal from the predicted model. The filter is reset after the detection of a step to improve post-event analysis. However, whether the method can determine the type of transient present and how it would perform on waveforms with slow

The authors gratefully acknowledge the financial support of the European Commission - Horizon 2020 program to the project Optimal System-Mix Of flexibility Solutions for European electricity (OSMOSE) (773406).

transitions (e.g., frequency ramps, amplitude modulations) is an open question.

Rather than rejecting or neglecting dynamic components, this paper proposes a technique to fully identify and characterize voltage or current waveforms in dynamic conditions. Building off of the study in [13], which presents the Functional Basis Analysis (FBA) algorithm for the identification of various signal dynamics, we have adapted the algorithm to better capture amplitude and phase step changes. The method employs a dictionary of parameterized signal models in order to identify the location and magnitude of step changes as well as characterize other dynamics in the signal. Furthermore, the improved method is able to detect interfering tones (e.g., harmonics and sub/inter-harmonics) as well as multiple steps within the same window. Finally, the proposed FBA technique has reduced computational cost as compared to the original version, making it suitable for eventual implementation in embedded devices (e.g., FPGAs) for real-time applications.

The paper is organized as follows: Section II presents the proposed algorithm for detection of common signal dynamics, multiple steps and interfering tones. Section III applies the FBA method to waveforms from three real-world grid events. The results are compared to both static and dynamic phasor estimation methods. Finally, Section IV concludes the paper with a discussion of the potential applications of the method.

II. Method

The objective of this paper is to identify and characterize step dynamics in power system signals for improved frequency and ROCOF analysis. To address the shortcomings of the phasor model briefly discussed in the introduction, the proposed method uses a generic model which incorporates common signal dynamics present in the grid, including amplitude steps (AS), amplitude modulations (AM), phase steps (PS) and frequency ramps (FR). The signal is generically modelled as:

$$x(t) = A_0(1 + g_A(t))cos(2\pi f_0 t + g_\phi(t) + \varphi_0) \tag{1}$$

where A_0, f_0 and φ_0 represent the fundamental amplitude, frequency and phase, respectively, and g_A and g_ϕ incorporate variations in the amplitude and phase, respectively. For the sake of nomenclature, the common signal dynamics mentioned above can be incorporated into (1) as follows:

$$\text{AS: } g_A(t) = k_a s(t - t_a) \tag{2}$$

$$\text{PS: } g_\phi(t) = k_p s(t - t_p) \tag{3}$$

$$\text{AM: } g_A(t) = k_m cos(2\pi f_m t + \varphi_m) \tag{4}$$

$$\text{FR: } g_\phi(t) = R\pi t^2 \tag{5}$$

where $s(t)$ is the step function, k_a and k_p are the step depths, t_a and t_p are the step locations within the window, k_m, f_m and φ_m represent the AM depth, frequency and phase, respectively, and R is the ramp rate in Hz/s.

Similar to how phasors are often represented as complex exponentials, (1) can be transformed into its analytic signal counterpart using the Hilbert Transform (HT). As is known, the HT is a linear operator that, for a generic time-varying signal $x(t)$, is defined as [14]:

$$\mathcal{H}[x(t)] = \frac{1}{\pi}\int_{-\infty}^{+\infty}\frac{x(\tau)}{t-\tau}d\tau = \frac{1}{\pi t} * x(t) \tag{6}$$

where $*$ indicates convolution. Combining the HT $\mathcal{H}[x(t)]$ with the original function yields the analytic signal $\hat{x}(t)$ which, due to the symmetry of the spectrum, contains only positive frequency components [14]:

$$\hat{x}(t) = x(t) + \boldsymbol{j}\mathcal{H}(x(t)). \tag{7}$$

Applying Euler's formula to the analytic form (7) allows for the representation of a real time-domain signal (1) as a complex exponential function:

$$\hat{x}(t) = A_0(1 + g_A(t))e^{j(2\pi f_0 t + g_\phi(t) + \varphi_0)} \tag{8}$$

which contains information on the signal envelope $x_A(t)$:

$$x_A(t) = |\hat{x}(t)| \tag{9}$$

The extraction of the signal envelope allows for independent analysis of this component, as discussed in the next sections.

A. Signal Analysis

For the identification and characterization of signal dynamics, we employ dictionaries of parameterized functions based on the signal models previously discussed. Fundamentally, dictionary analysis involves projection of the input vector (i.e., a sampled, windowed signal) onto a functional basis of vectors defined by parameterized signal models. The kernel that best matches the input signal is identified and its corresponding parameters and model are used to reconstruct the input signal. Though detailed in the following sections, a brief summary of the main steps involved are as follows:

1) The signal envelope is analyzed using dictionaries of amplitude modulations and amplitude steps.
2) The full analytic signal is analyzed for phase steps with a predefined PS dictionary.
3) The identified elements (i.e., the estimated envelope and phase steps) are incorporated as fixed components into a time-domain FR dictionary. The input signal is analyzed with this adapted dictionary to identify the fundamental frequency, ramp rate and initial phase.

The above structure of the FBA algorithm has been developed through several iterations to capture progressively more complex signals. Analysis of the envelope allows for identification of amplitude dynamics, independent of other signal variations (e.g., frequency ramps, phase steps). Projection of the analytic signal onto a PS dictionary is necessary for identification of one or more phase steps. Finally, a FR dictionary was found to be extremely sensitive to the presence of other signal dynamics, hence the need to include these identified components in the dictionary kernels. These steps are thoroughly explained in Algorithm 1.

1) Envelope Analysis: Given a discrete, sampled signal $x(t_l)$ for $l = 1...L$ with an unknown mathematical model, the analytic form $\hat{x}(t_l)$ first needs to be approximated by means of a filter with a magnitude response of nearly 0 dB for positive frequencies and large attenuation (e.g., -120 dB) for the negative frequency domain. The signal envelope $x_A(t_l)$ can be approximated by modulations or steps in the amplitude: $x_A(t_l) = A_0(1 + k_m cos(2\pi f_m t_l + \varphi_m)$ or $x_A(t_l) = A_0(1 + k_a s(t_l - t_a))$, respectively.

The corresponding AM dictionary is therefore defined for all combinations of the frequency f_m and phase φ_m parameters:

$$d_{i,AM}(f_m, \varphi_m) = a_i DFT[cos(2\pi f_m t_l + \varphi_m)] \tag{10}$$

where a_i is a coefficient that normalizes the kernel and DFT indicates the Discrete Fourier Transform with coefficients for bins $k = 1...K$ defined as:

$$X(k) = DFT[x(t_l)] = \sum_{l=0}^{L-1} x(t_l) W_L^{kl} \tag{11}$$

where $W_L^k = e^{-j2\pi k/L}$ is the k-th root of unity modulo L. Each kernel is then fully determined by the parameter set $\gamma(f_m, \varphi_m)$ and signal model of the envelope for a sampled window t_l where $l = 1...L$. The parameter sets $\gamma_{AM} = [f_m, \varphi_m]$ are selected to best capture common signal dynamics in power grids (e.g., $f_m \in [0, 5]Hz$). The parameter set resolutions are also user-defined and depend on performance requirements and the computational cost of the algorithm.

Similarly, the kernels of the AS dictionary are defined for different step locations t_a within the window:

$$d_{i,AS}(t_a) = a_i DFT[s(t_l - t_a)] \tag{12}$$

Note that the DFT of the envelope is used rather than the time-domain waveform since this allows for the compression of the signal into a reduced set of Fourier coefficients. Examination of these coefficients yields the remaining model parameters, such as the scaling factor of the dynamic (i.e., $A_0 k_a$ or $A_0 k_m$) and the DC shift (i.e., A_0). It is important to note that the kernels in the AM and AS dictionaries are defined for frequency ranges that exclude the DC component (i.e., $k = 2...K$). This exclusion means that projection of an input envelope onto this dictionary yields the scaling factor of the dynamic.

In lines 4-7 of Algorithm 1, the frequency spectrum of the signal envelope is first computed and curtailed to the appropriate frequency range (e.g., 0 to 100 Hz). This range is user-defined and selected to best capture the signal dynamics of interest. The DC component is separated ($X_{A,DC}$) while the remaining frequency bins are normalized by either the length of the window L or the norm of the vector (i.e., $a = ||X_{full}(k = 2...K)||_2^{-1}$) to yield X_A and $\bar{X}_A$, respectively. The latter is then projected onto all kernels in the AM (line 8) and AS (line 17) dictionaries to construct a scaled and rotated approximation of the input signal $(d_i^H \bar{X}_A) d_i$. The kernel that minimizes the difference between this approximation and the input vector is then identified (for more details see [13]). The corresponding parameter sets for AM and AS are recorded in lines 9 and 18, respectively.

In lines 10-11 and 19-20, the parameter sets γ_{AM}^* and γ_{AS}^* and the vector X_A are used to calculate the combined scaling factors, $c_{AS} = k_s A_0$ and $c_{AM} = k_m A_0$. A_0 is then computed in lines 12-13 and 21-22 by removing the spectral leakage due to the presumed dynamic ($X_2(k = 1)$) from the DC component $X_{A,DC}$. With A_0, the combined scaling factors, c_{AM} and c_{AS}, can be used to identify k_m and k_s in lines 14 and 23, respectively.

The envelopes are reconstructed in lines 15 and 24 and compared to $x_A(t)$ using the time-domain error (TDE) metric:

$$TDE(x^*, x) = \frac{||x^*(t_l) - x(t_l)||_2}{L}, \tag{13}$$

where x^* is the estimated component and x is the reference or input signal. The envelope with the smaller TDE is reported as the most likely amplitude dynamic $x_A^*(t)$ in line 26.

2) PS Detection: For PS identification, a dictionary is predefined for parameter sets $\gamma_{PS} = [f_0, k_p, t_p]$:

$$d_{i,PS}(f_0, k_p, t_p) = a_i DFT[exp(j(2\pi f_0 t_l + k_p s(t_l - t_p)))] \tag{14}$$

The kernels for this dictionary are limited to a user-defined frequency range (e.g., $k = 1...K$). The frequency spectrum of the analytic signal $\hat{X}$ is projected onto the PS dictionary in line 29 and the best matching kernel with parameter set γ_{PS}^* is identified. If detected, the PS component is saved as $x_\phi^*(t_l)$.

3) FR Detection: Using the reconstructed signal envelope $x_A^*(t_l)$ and the identified PS component $x_\phi^*(t_l)$, an adapted time-domain dictionary is constructed in line 32 for different fundamental frequency and ramp rate combinations:

$$d_{i,FR}(f_0, R) = x_A^*(t_l) e^{j(2\pi f_0 t_l + R\pi t_l^2 + x_\phi^*(t_l))} \tag{15}$$

The filter-approximated analytic signal $\hat{x}(t_l)$ is projected onto each dictionary kernel to find the rotation coefficient:

$$c_\phi = \frac{d_i^H \hat{x}}{||d_i^H \hat{x}||_2} \tag{16}$$

which embeds the phase offset $\varphi_0 = \angle c_{\varphi_0}$. The phase-shifted kernel is compared to the original signal and the closest matching parameter set is identified in line 34. Finally, all model components of the signal have been identified and are used to reconstruct the time-domain waveform in line 36.

B. Detection of Multiple Steps

Thus far, the algorithm discussed is designed to be applied to an observation window with a single step. In the case where multiple amplitude and/or phase steps occur in the same window, additional measures must be taken. An assumption is made that the first step is identified when it first enters the window and that two steps do not arrive in the observation window within the same reporting period (i.e., the steps do not occur within one reporting period T_r of each other).

Once an AS/PS is identified, the magnitude is recorded and its location is tracked as the window slides so that, in the

Algorithm 1 Functional Basis Analysis Algorithm

1: **Input:** signal $x(t_l)$, D_{AM}, D_{AS}, D_{PS}
2: $\hat{x}(t_l) = Filter[x(t_l)]$, $x_A(t_l) = |\hat{x}(t_l)|$
3: Remove previous amplitude/phase steps

Envelope Analysis

4: $X_{A,full} = DFT[x_A(t_l)]$
5: $X_A = X_{A,full}(k = 2...K)/L$
6: $\bar{X}_A = aX_{full}(k = 2...K)$
7: $X_{A,DC} = X_{full}(k = 1)/L$

AM Detection:

8: Project onto kernels d_i in dictionary D_{AM}
9: $[i^*] = \arg\min_i[||d_i^H \bar{X}_A d_i - \bar{X}_A||_2]$
$\rightarrow \gamma^*_{AM} = [f_m(i^*), \varphi_m(i^*)]$
Calculate scaling factor ($k_m A_0$)
10: $X_{AM,1} = DFT[sin(2\pi f^*_m t_l + \varphi^*_m)]/L$
11: $c_{AM} = |X^H_{AM,1} X_A|$
Calculate DC shift (A_0)
12: $X_{AM,2} = DFT[c_{AM} sin(2\pi f^*_m t_l + \varphi^*_m)]/L$
13: $A^*_0 = X_{A,DC} - X_{AM,2}(k = 1)$
14: $k^*_m = c_{AM}/A^*_0$
15: $x^*_{AM} = A^*_0(1 + k^*_m sin(2\pi f^*_m t_l + \varphi^*_m))$
16: Compute $TDE(x_{AM}, x_A)$

AS Detection:

17: Project onto kernels d_i in dictionary D_{AS}
18: $[i^*] = \arg\min_i[||d_i^H \bar{X}_A d_i - \bar{X}_A||_2]$
$\rightarrow \gamma^*_{AS} = [t_a(i^*)]$
Calculate scaling factor ($k_a A_0$)
19: $X_{AS,1} = DFT[s(t_l - t^*_a)]/L$
20: $c_{AS} = |X^H_{AS,1} X_A|$
Calculate DC shift (A_0)
21: $X_{AS,2} = DFT[c_{AS} s(t_l - t^*_a)]/L$
22: $A^*_0 = X_{A,DC} - X_{AS,2}(k = 1)$
23: $k^*_a = c_{AS}/A^*_0$
24: $x^*_{AS} = A^*_0(1 + k^*_a s(t_l - t^*))$
25: Compute $TDE(x_{AS}, x_A)$
26: TDE comparison $\rightarrow x^*_A(t_l)$

PS Detection:

27: $\hat{X}_{full} = DFT[\hat{x}(t_l)]$
28: $\hat{X} = \hat{X}_{full}(k = 1...K)$
29: Project onto kernels $d_i(f_0, k_p, t_p)$ from dictionary D_{PS}
30: $[i^*] = \arg\min_i[||d_i^H \hat{X} d_i - \hat{X}||_2]$
$\rightarrow \gamma^*_{PS} = [f_0(i^*), k_p(i^*), t_p(i^*)]$
31: $x^*_\phi(t) = k^*_p s(t_l - t^*_p)$

FR Detection:

32: Create dictionary $D_{FR}(f_0, R)$
33: Project onto kernels $d_i(f_0, R)$ from dictionary D_{FR}
34: $[i^*] = \arg\min_i[||c_{\varphi_0} d_i - \hat{x}||_2]$
$\rightarrow \gamma^*_{FR} = [f_0(i^*), R(i^*)]$
35: $\varphi^*_0 = \angle c^*_{\varphi_0}$
Reconstruct full signal
36: $x_{est}(t_l) = x^*_A(t_l) cos(2\pi f^*_0 t_l + R^* \pi t_l^2 + x^*_\phi(t_l) + \varphi^*_0)$
37: Compute $TDE(x_{est}(t_l), x(t_l))$

consecutive window, the new step location is known to be at $(t^* - T_r)$. For detection of any new steps, the impact of all previous steps must be removed, as indicated in line 3. Note that if no additional steps are found, then the approximation of the previous steps can be reevaluated and improved. This reduces the chance of parameter error being propagated, which may be the case for a step that first appears at the very end of the window.

If the previous step includes an AS, then the signal envelope must be modified to remove its effects:

$$x_A(t_l) = \frac{x_A(t_l)}{1 + k^*_{a1} s(t_l - t^*_{a1})} \tag{17}$$

The envelope is then analyzed normally in lines 8-26. The detected magnitude of the second step and the reconstructed envelope must be adjusted again by the first step:

$$x^*_A(t_l) = x^*_A(t_l)(1 + k^*_{a1} s(t_l - t^*_{a1})) \tag{18}$$

$$k^*_{a2} = k^*_{a2}(1 + k^*_{a1} s(t_l - t^*_{a1})) \tag{19}$$

If the previous step involves a PS, then it must be removed from the analytic signal before further PS analysis is done:

$$\hat{x}(t_l) = \frac{\hat{x}(t_l)}{e^{jk^*_{p1} s(t_l - t^*_{p1})}} \tag{20}$$

For the FR dictionary analysis in lines 32-36, the model should contain all known AS and PS still present in the window (e.g., $x^*_\phi(t_l) = k^*_{p1} s(t_l - t^*_{p1}) + k^*_{p2} s(t_l - t^*_{p2})$).

C. Detection of Interfering Tones

Following the occurrence of a fault or other disruption in the grid, additional signal tones may appear in the measured waveform, corresponding to a harmonic response or the resonance frequency of the grid. The following steps are performed to identify an interfering tone:

1) Algorithm 1 provides a first estimate of the underlying signal dynamic (without any additional tones).
2) The extracted signal model $x^1_{est}(t_l)$ is removed from the original signal $x(t_l)$, leaving the remainder which contains the additional tone $x_r(t_l) = x(t_l) - x^1_{est}(t_l)$.
3) $x_r(t_l)$ is analyzed by a single tone extraction method (e.g., interpolated DFT), with a 10% relative amplitude threshold, to approximate the tone $x^*_r(t_l)$.
4) $x^*_r(t_l)$ is removed from the original signal $x(t_l)$ and analysis with the FR dictionary is repeated to yield a second estimate, $x^2_{est}(t_l)$.
5) These steps can be repeated for a specified number of iterations or until changes in the time-domain error are below a given threshold.

D. Computational Complexity

The computational complexity of each step in Algorithm 1 is presented in Table I where N is the number of kernels in each dictionary, L represents the number of samples in the signal, and K is the number of frequency bins analyzed. Calculating the frequency spectrum depends on the method used (e.g., FFT, DFT) and, therefore, the computational complexity

is represented as ζ. The size of the dictionaries required is significantly reduced as compared to the method presented in [13]. For instance, the AS dictionary is only a function of the parameter t_a as opposed the parameter set $[f_0, k_a, t_a]$ which simplifies analysis. Finally, AM, AS and PS detection are independent operations which can be done in parallel on FPGA-based (Field Programmable Gate Array) devices to improve computational throughput.

TABLE I
COMPUTATIONAL COMPLEXITY OF SCD METHOD PRESENTED IN ALGORITHM 1

Dynamic	Operation	Complexity
AM and AS	Projection	$\mathcal{O}(KN)$
	Scaling Factor	$\mathcal{O}(L+\zeta+K)$
	DC Shift	$\mathcal{O}(L+\zeta)$
PS	Projection	$\mathcal{O}(KN)$
FR	Create D_{FR}	$\mathcal{O}(LN)$
	Projection	$\mathcal{O}(LN)$

III. EXPERIMENTAL VALIDATION

To evaluate the performance of the proposed algorithm, we applied it to waveforms from 3 grid events and compared the results to both *static* and *dynamic* phasor estimation methods. For the former, we selected a 3-point iterative Interpolated DFT (i-IpDFT) algorithm [15] with a Hann window and negative spectrum compensation which is compliant with P and M class requirements [3]. For dynamic phasor analysis, we used the Compressed Sensing Taylor-Fourier multifrequency (CSTFM) method [9] which captures the 1^{st} and 2^{nd} order derivatives of the phasor. The parameter sets for the FBA dictionaries presented in Table II were selected to capture the range of common signal dynamics in power systems. All methods were applied to the waveforms using a 100 ms window and 50 frames per second (fps) reporting rate such that the results are reported for overlapping windows. While shorter windows are preferable for analysis of waveforms with rapidly changing parameters, 100 ms was found to be the minimum length needed to accurately characterize slower dynamics like FR and AM. Finally, the ROCOF, frequency and parameter error are examined for the cases with known ground truth values. In real-world scenarios, however, only the TDE is available as an indicator of how well the model matches the input signal. Therefore, even though phasor-based methods are not intended for point-on-wave reconstruction, this metric will be provided for comparison.

A. California Grid Event 2016

The first case examined involves a fault in the California grid in 2016 caused by a wildfire. The fault resulted in a series of phase steps causing the inverters connecting a number of solar power plants to trip due to erroneous instantaneous frequency estimates, cutting 700 MW of generation [16]. A single phase voltage waveform from the event was analyzed and found to contain a 26° phase shift and 39.5% amplitude dip. Approximately 41.3 ms later, the waveform reverted to base parameters. Using these parameters, identified in [16], the signal was reconstructed at 60 Hz with an amplitude of 1 p.u., sampling frequency of $F_s = 50$ kHz and 60 dB of white Gaussian noise as shown in Figure 1. To clarify, the known step parameters are used as reference values for evaluation of performance but are unknown by FBA algorithm which processes the input waveform blindly.

TABLE II
PARAMETER SETS FOR FBA DICTIONARIES

Dictionary	Parameter	Resolution	Range
PS	f_0 (Hz)	0.04	[49,51]
	k_p (rad)	0.014	$\pm[\pi/18, 5\pi/18]$
	t_p (ms)	0.4	$[5, T_w - 5]$
FR	f_0 (Hz)	0.02	[49,51]
	R (Hz/s)	0.2	$[-10, 10]$
AS	t_a (ms)	0.4	$[5, T_w - 5]$
AM	f_m (Hz)	0.165	$[0.2, 5]$
	φ_m (rad)	0.216	$[0, 2\pi]$

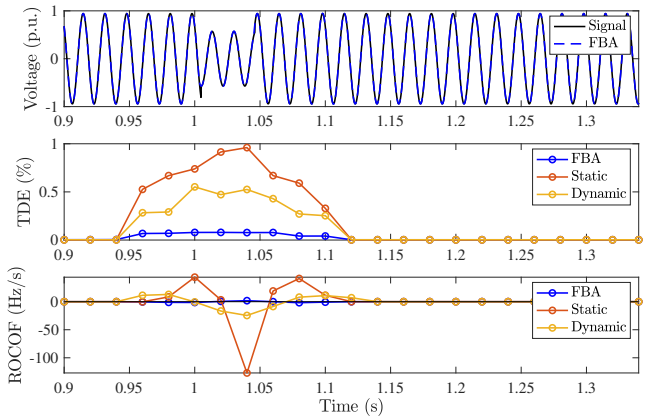

Fig. 1. California event 2016 [16]: (top) signal and reconstructed waveform, (middle) TDE and (bottom) ROCOF reported by all methods.

The FBA dictionaries were adjusted to a 60 Hz nominal frequency (e.g., 59 to 61 Hz range) and 120 ms window. As shown in Figure 1, the static and dynamic phasor methods are unable to account for the variation in the waveform, resulting in an order of magnitude difference in the TDE metric relative to the FBA results. The maximum TDE for each method, represented as a percentage of the amplitude 1 p.u., is 0.96% (static), 0.55% (dynamic) and 0.079% (FBA). Furthermore, the frequency and ROCOF values reported phasor-based methods are highly disturbed by the presence of amplitude and phase steps, with spikes of -43.6 Hz/s (static) and -12.8 Hz/s (dynamic). In contrast, the FBA method maintains a steady approximation of the ROCOF with a maximum value of 1.8 Hz/s. As this is a synthetic signal, we can compare these values to the true ROCOF of 0 Hz/s. Finally, the FBA method accurately identifies and tracks the location and magnitude of the two steps in the window, as reported in Table III. No interfering tones were identified in this signal.

TABLE III
MEAN STEP PARAMETER ERROR AS APPROXIMATED BY THE FBA.

		k_a (%)	k_p (%)	t_a/t_p (ms)
California	Step 1	0.4	4.5	1.6
	Step 2	2.8	2.1	0.8
Bornholm	Step 1	2.1	1.3	0.3
	Step 2	2.4	4.9	1.3

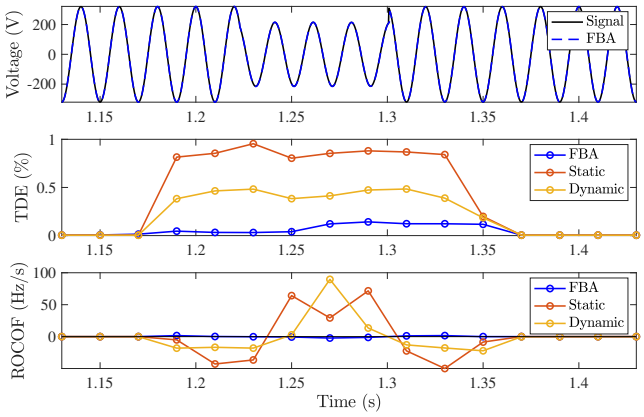

Fig. 2. Bornholm grid event [17]: (top) signal and reconstructed waveform, (middle) TDE and (bottom) ROCOF reported by all methods.

B. Bornholm Grid Event 2018

The second case involves data from a study of LOM triggered events in the Bornholm Island, a power network with a large portion of renewable energy and a single interconnection to the Nordic power grid [17][1]. The study found that a number of false ROCOF triggers were due to phase shifts in the waveforms rather than underlying frequency dynamics. The waveform analyzed in Fig. 2 demonstrates an example fault on February 2nd, 2018, as recorded by a metrology grade digitizer installed in a LV substation on the Bornholm Island. A fitting of the waveform, provided by [17], reveals that an amplitude dip of 33% and phase shift of -0.4 rad occurs then recovers after a few cycles (e.g., $k_{a1} = -0.33$, $k_{a2} = 0.33$, $k_{p1} = -0.4$ rad, $k_{p2} = 0.4$ rad). There is no significant underlying frequency change, despite what phasor-based methods report.

As in the California case, the static and dynamic phasor methods are incapable of capturing the signal, yielding maximum TDE (relative to the nominal 230 V) of 0.95% and 0.48%, respectively. In contrast, the FBA method can detect and incorporate the phase and amplitude steps into the model such that the maximum TDE is 0.14%. The phasor methods also report large ROCOF deviations of up to 71.6 Hz/s (static) and 89.6 (dynamic). In contrast, the FBA technique yields a maximum ROCOF of -2.2 Hz/s. The parameter errors for the phase and amplitude steps are shown in Table III. No interfering tones were identified in this signal.

[1]For project details see http://www.rocofmetrology.eu/rocof-measurements-on-bornholm-green-island/

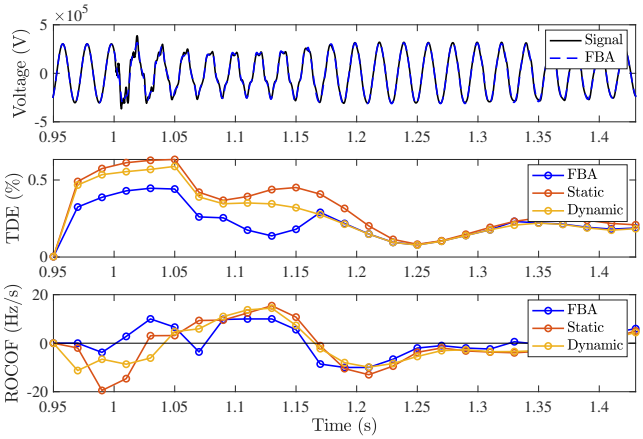

Fig. 3. Adapted IEEE 39-bus grid event [2]: (top) signal and reconstructed waveform, (middle) TDE and (bottom) ROCOF reported by all methods.

C. IEEE 39-Bus Fault Simulation

The final case study involves simulations of an adapted version of the standard IEEE 39-bus test system in [2]. The model involves 39 buses with 19 loads, 10 synchronous generators, and an additional 4 wind generators. The waveform analyzed in Figure 3 is due to the tripping of 1.5 GW of generation, as simulated in MATLAB Simulink and Opal-RT eMEGAsim RTS [2].

The maximum TDE for each method, relative to the nominal voltage of 345 kV, is 0.63% (static), 0.59% (dynamic) and 0.44% (FBA). The FBA method yields an average 4.2 kV and 3.8 kV decrease in point-by-point time domain error of the static and dynamic methods, respectively. While the ROCOF values are harder to verify since the ground truth is unknown, the time-domain error indicates a better fit of the original signal. A small phase step on the order of $-\pi/18$ is identified around 1 s. Finally, the FBA method also identifies an interfering tone at 196 Hz and 15% magnitude which was confirmed by frequency analysis of the waveform.

IV. CONCLUSION

This paper presents an algorithm for the detection and characterization of one or more amplitude and/or phase steps in a power system waveform, as well as the identification of other common signal dynamics (e.g., interfering tones, frequency ramps, amplitude modulations). The FBA technique is shown to improve time-domain signal reconstructions and frequency and ROCOF estimations during real-world grid events. For this reason, potential applications would include LOM protection schemes and UFLS operations. Next steps in this research will involve implementation of the technique in an FPGA device for real-time applications and validation.

REFERENCES

[1] G. Rietveld, P. S. Wright, and A. J. Roscoe, "Reliable Rate-of-Change-of-Frequency Measurements: Use Cases and Test Conditions," *IEEE Trans. on Instr. and Meas.*, vol. 69, no. 9, pp. 6657–6666, 2020.

[2] Y. Zuo, G. Frigo, A. Derviškadić, and M. Paolone, "Impact of Synchrophasor Estimation Algorithms in ROCOF-Based Under-Frequency Load-Shedding," *IEEE Trans. on Power Systems*, vol. 35, no. 2, pp. 1305–1316, 2020.

[3] "IEEE Standard for Synchrophasor Measurements for Power Systems, Amendment 1: Modification of Selected Performance Requirements," *IEEE Std C37.118.1a-2014*, pp. 1–25, 2014. DOI: 10 . 1109 / IEEESTD.2014.6804630.

[4] I. Kamwa, S. R. Samantaray, and G. Joos, "Compliance Analysis of PMU Algorithms and Devices for Wide-Area Stabilizing Control of Large Power Systems," *IEEE Transactions on Power Systems*, vol. 28, no. 2, pp. 1766–1778, 2013. DOI: 10 . 1109 / TPWRS . 2012 . 2221168.

[5] G. Frigo *et al.*, "Definition of Accurate Reference Synchrophasors for Static and Dynamic Characterization of PMUs," *IEEE Trans. on Instr. and Meas.*, vol. 66, no. 9, pp. 2233–2246, 2017.

[6] A. J. Roscoe *et al.*, "The Case for Redefinition of Frequency and ROCOF to Account for AC Power System Phase Steps," in *2017 IEEE International Workshop on Applied Meas. for Power Systems (AMPS)*, 2017, pp. 1–6.

[7] H. Kirkham and A. Riepnieks, "Dealing with non-stationary signals: Definitions, considerations and practical implications," in *2016 IEEE Power and Energy Society General Meeting (PESGM)*, 2016, pp. 1–5.

[8] J. A. de la O Serna, "Dynamic Phasor Estimates for Power System Oscillations," *IEEE Transactions on Instrumentation and Measurement*, vol. 56, no. 5, pp. 1648–1657, 2007. DOI: 10.1109/TIM.2007.904546.

[9] M. Bertocco, G. Frigo, C. Narduzzi, C. Muscas, and P. A. Pegoraro, "Compressive Sensing of a Taylor-Fourier Multifrequency Model for Synchrophasor Estimation," *IEEE Trans. on Instr. and Meas.*, vol. 64, no. 12, pp. 3274–3283, 2015.

[10] J. Barros, M. de Apráiz, and R. I. Diego, "A wavelet-based transient detector for P and M class phasor measurement unit integration," in *2017 IEEE International Workshop on Applied Meas. for Power Systems (AMPS)*, 2017, pp. 1–6.

[11] J. Ren and M. Kezunovic, "An Adaptive Phasor Estimator for Power System Waveforms Containing Transients," *IEEE Transactions on Power Delivery*, vol. 27, no. 2, pp. 735–745, 2012. DOI: 10.1109/TPWRD.2012.2183896.

[12] M. de Ápraiz, R. I. Diego, and J. Barros, "Transient detection in phasor measurement units with Kalman filtering," in *2018 18th International Conference on Harmonics and Quality of Power (ICHQP)*, 2018, pp. 1–6. DOI: 10.1109/ICHQP.2018.8378920.

[13] A. Karpilow, A. Derviškadić, G. Frigo, and M. Paolone, "Characterization of non-stationary signals in electric grids: A functional dictionary approach," *IEEE Trans. on Power Systems*, 2021.

[14] S. L. Hahn, "Hilbert transforms in signal processing," *Artech House*, 1996.

[15] A. Derviškadić, P. Romano, and M. Paolone, "Iterative-Interpolated DFT for Synchrophasor Estimation: A Single Algorithm for P- and M-Class Compliant PMUs," *IEEE Trans. on Instr. and Meas.*, vol. 67, no. 3, pp. 547–558, Mar. 2018, ISSN: 0018-9456.

[16] NERC, "1,200 MW Fault Induced Solar Photovoltaic Resource Interruption Disturbance Report," NERC, Tech. Rep., 2017.

[17] P. S. Wright, P. N. Davis, K. Johnstone, G. Rietveld, and A. J. Roscoe, "Field Measurement of Frequency and ROCOF in the Presence of Phase Steps," *IEEE Trans. on Instr. and Meas.*, vol. 68, no. 6, pp. 1688–1695, 2019.